

Integrated controller design for rejecting load distribution disturbance in collision avoidance

Abdullah Zulkifli^{1,3*}, Mohamad Heerwan Peeie^{1,3*}, M. Izhar Ishak^{1,3}, Muhammad Aizzat Zakaria^{2,3}

¹Faculty of Mechanical and Automotive Engineering Technology, Universiti Malaysia Pahang Al-Sultan Abdullah, 26600 Pahang, Malaysia

²Faculty of Manufacturing and Mechatronic Engineering Technology, Universiti Malaysia Pahang Al-Sultan Abdullah, 26600 Pekan, Pahang, Malaysia

³Centre for Automotive Engineering, Universiti Malaysia Pahang Al-Sultan Abdullah, 26600 Pekan, Pahang, Malaysia

Abstract - A collision avoidance (CA) system has become a necessity in every vehicle due to its ability to prevent collisions. Numerous techniques have been developed to improve the tracking system, thereby reducing the possibility of collision by increasing its accuracy relative to the reference signal. The path-tracking system is an important element in the CA system, whose function is to prevent deviation from the reference path. However, a conventional path-tracking system without an estimator is unable to track the reference signal in the presence of an external load disturbance. Moreover, the vehicle velocity, as well as variations in load disturbance, retard the vehicle's path tracking abilities while avoiding an obstacle. This deficiency can lead to fatal consequences during vehicle navigation due to understeering and oversteering. The primary purpose of this research is to design an integrated controller for a disturbance-rejection (IC-DR) path-tracking system to improve tracking performance by rejecting external disturbances while avoiding obstacle. The design process involved formulating a longitudinal force controller to track changes in vehicle acceleration during the CA scenario. Then, the lateral controller was formulated by following these orders: (1) Linearization of the model, (2) Optimal state estimator design by using a linear model, (3) Optimal state feedback regulator design. The CA scenario was simulated by using a nonlinear tire characteristic for vehicle model development in MATLAB Simulink. Next, both controllers were integrated with the vehicle system, and their performance was analyzed. The simulation results show that the path-tracking system prevents deviation from the reference trajectory in understeering and oversteering situations. The proposed path-tracking method can efficiently reduce external disturbances, and it is much simpler than other advanced controllers. The results show that by implementing IC-DR, the mean squared-error between the vehicle and reference trajectories is below 0.01 for all additional load disturbance percentages at different velocities.

Article History

Received : 27 November 2024

Revised : 21 September 2025

Accepted : 19 January 2026

Published : 30 June 2026

Keywords

Integrated controller for disturbance rejection

Optimal control

Collision avoidance system

Linear Kalman state estimator

Longitudinal and lateral controller

Path tracking system

1. Introduction

Optimizing road safety requires understanding the preventable factors that cause traffic fatalities [1]. Traffic accidents are a leading cause of mortality in Malaysia and other developing countries. According to the World Health Organization, road traffic casualties are the ninth most frequent cause of death globally [2]. Collision avoidance (CA) technologies can help drivers reduce the likelihood of accidents and ensure passenger safety [2]. Applications of CA include longitudinal and lateral control in driving circumstances. Active collision avoidance system (ACAS) is a crucial component of all active safety measures [3]. By gathering environmental data such object range, location, and speed, contemporary info and sensor systems are used to increase drivers' sense of awareness. After that, collision possibility is analyzed using all available data so that appropriate action can be taken to prevent accidents in risky scenarios [4]. There are various CA techniques and they are classified into three categories: (1) longitudinal braking [5], (2) evasive steering [6], and (3) compound collision avoidance system [7].

CA systems are one of the most intricate systems in the autonomous driving assistance system (ADAS) family. It assists the vehicle in preventing collision. There are essentially three submodule strategies: Path Planning, Threat Assessment [8], and Path Tracking Strategy [9]. Accident chance is mostly calculated by Threat Assessment. The Path Planning then receives the signal and replans the existing route into a better one. The route approach will regulate the replanned movement value to reach the target value. As real-world collisions typically include a vehicle travelling at a high speed, carefully choosing each method is necessary to ensure that a viable collision avoidance execution is achieved [10]. In an emergency, the CA system would operate to guide the car with the use of low-level actuators like the steering and brakes. The decision-making strategy determines the appropriate actuation that the vehicle will take, such as braking, steering, or throttle control intervention [11 - 12].

The Path Tracking Strategy must employ a definite decision-making method to produce the appropriate interference. This is because various situations call for unique evasive techniques. A straightforward, linear tracking system with a fast response time is typically referred to as a single-input, single-output system (SISO). It is demonstrated in [13] by one distinct controller producing one distinct low-level action. In previous studies [14 - 15], vehicle velocity and yaw rate

were the input of the low-level control, whereas deceleration and steering angle were the output. The complicated input–output connection and nonlinear characteristics of the mobile robots and the host vehicle were not fully acknowledged. Recognizing multiple-input and multiple-output (MIMO) route tracking techniques that incorporate all vehicle restraints into the computation has been the focus of current efforts. Due to the unpredictable nature of CA maneuvers, the authorized controller approach must function as an automatic command for the vehicle in all capacity danger scenarios. If the host vehicle and an obstruction share the moving axis, the chosen avoidance system must command evasive steering to avoid collision. In a dangerous situation, the host vehicle’s braking system must be available to support the CA system when it moves in a different direction from the obstacles.

Finding the best compromise between ride comfort, stability, and vehicle handling has been the focus of much vehicle system dynamics research in recent years [16]. Better methods are required now since the issues are clearly visible in the cases of contemporary vehicles. For large sedans and luxury vehicles, achieving exceptional ride quality is contingent upon attaining suitable handling characteristics. Meanwhile, sports cars have excellent handling capabilities but fall short in terms of comfortable ride quality. To satisfy consumer needs, car manufacturers have a wide range of alternatives for alterations in the design stage. The three main goals to be considered are vehicle control, passenger comfort, and the design point of view. Potholes and other disturbances in the road should be addressed without sacrificing passenger comfort [17]. During the control stage, these characteristics are typically taken into account by either preventing excessive rolling and pitching of the vehicle’s body or by ensuring that the tires have adequate contact with the road [17]. Any increase in mass on either side of the car impacts its stability. Researchers frequently focus exclusively on vehicle mass while conducting their studies, but this is inadequate because vehicles also carry either passengers or cargo [16]. The forces operating on each tire can be impacted by how the increased weight is distributed across the vehicle, which can then affect its stability and characteristics.

In situations where the system is disturbed or has uncertainties in the model, an optimal control approach is frequently employed [18]. A previous study compared linear quadratic gaussian (LQG) and model predictive controller (MPC) for steering control systems [19] and concluded that LQG is more compact and requires less computing power, while MPC requires a lot of maintenance and is not as stable. Another study compared the quadrotor linear quadratic regulator (LQR) and LQG performance [17]. Though LQR cannot track noise and disturbance, it responds quickly despite not providing estimation or an integral portion. LQG exhibits excellent controllability. A sequential LQG strategy has been used for solving nonlinear tracking issues [18]. The LQG controller’s versatility, resilience, and high control accuracy are demonstrated by the outcomes of MATLAB computation. Another study [18] investigated the performance of the vehicle’s tracking trajectory by using LQG with adaptive Q-matrix. The results showed that the vehicle achieved smooth tracking even with model uncertainty and noise [18]. When sensor noise is added, states can be estimated and controlled using this method. The sensor must, however, adhere to real-time restrictions for that to happen. One study presented the LQG controller development and modeling for the vehicle, showing that the stability of the closed loop system can be attained through this technique [20].

Nevertheless, many trajectory design techniques in use now are stagnant without including disturbance or uncertainty of the vehicle model, especially in extreme maneuvering conditions. Investigating dynamic trajectory design procedures for an efficient autonomous vehicle’s (AVs) overtaking challenge while considering several real-world field conditions is imperative to satisfy the expectations of real-world applications [21]. One of the disturbances is additional load distribution, which acts on the vehicle and can affect its stability during navigation [16]. Hamid et al. [22] investigated collision avoidance system with various loads. Although the proposed path tracking system, which is nonlinear model predictive controller (NMPC), managed to track the reference path, the algorithm complexity needs to be considered for quick actuator response in real-time application [23]. The study only focused on where the load variation is: (i) estimated weight at the curb (vehicle plus driver), (ii) occupants with five seats, which added 20% to the vehicle’s weight, and (iii) individuals who are completely seated and carrying bags, which added 36% to the vehicle’s weight [22]. However, the study did not fully associate the estimated load variation with real-time application as the weight percentages do not represent the exact location of weight distribution corresponding to the location of passenger seat. Thus, this study will fill the gap of past studies by implementing the additional weight directly on the right or left part of the tire in nonlinear vehicle dynamic model as well as designing the overtaking path tracking with light computational burden without neglecting vehicle dynamics.

To address this issue, a combination of longitudinal force controllers with lateral controllers was designed to reject the effect of load distribution disturbance while avoiding an obstacle. The lateral controller was designed by using optimal control theory for both estimator and regulator for converging the measured state into zero by referring the state from reference generator. It also produces a feasible actuator that corresponds to the error between the state of estimator with the reference generator. The performance of the proposed controller was evaluated using simulation in MATLAB Simulink with nonlinear vehicle model. The collision avoidance scenario was simulated with the additional load being added at each tire for 30, 40, and 50 km/h. The proposed controller was employed in nonlinear vehicle model during collision avoidance scenario to prevent vehicle’s instability due to load transfer phenomena.

2. Materials and Methods

2.1 Nonlinear Vehicle Dynamic Model

Figure 1 illustrates the longitudinal, lateral, and yaw motion and can be expressed as in Eq.s 1, 2 and 3, respectively. The variables m , \ddot{x} , \ddot{y} , \dot{x} , \dot{y} , $\dot{\phi}$ represent key aspects of vehicle dynamics: vehicle’s total mass, longitudinal and lateral acceleration, longitudinal and lateral velocity, and the rate of body angle, respectively [2]. Understanding these elements

is essential for analyzing vehicle performance and safety. $F_{xfl}, F_{xfr}, F_{xrl}, F_{xrr}$ and $F_{yfl}, F_{yfr}, F_{yrl}, F_{yrr}$ represent the longitudinal and lateral forces at the front left, front right, rear left, and rear right tires, accordingly [16]. Additionally, l_f and l_r are the distances from the center of gravity (CG) to the front and rear tires, accordingly [16]. Meanwhile, d_w stands for the track width. F_{ax} is the actuator force to drive the system in longitudinal motion. F_{ax} can be expressed as in Eq. 26 in Section 4.0.

$$m\ddot{x} = F_{ax} - (F_{xfl} + F_{xfr}) \cos \delta + F_{xrl} + F_{xrr} - (F_{yfl} + F_{yfr}) \sin \delta + m\dot{\phi}\dot{y} \tag{1}$$

$$m\ddot{y} = F_{yrl} + F_{yrr} + (F_{xfl} + F_{xfr}) \sin \delta + (F_{yfl} + F_{yfr}) \cos \delta - m\dot{\phi}\dot{x} \tag{2}$$

$$I_z\ddot{\phi} = l_f(F_{xfl} + F_{xfr}) \sin \delta + l_f(F_{yfl} + F_{yfr}) \cos \delta - l_r(F_{yrl} + F_{yrr}) + \frac{d_w}{2}(F_{xfr} - F_{xfl}) \cos \delta + \frac{d_w}{2}(F_{xrr} - F_{xrl}) + \frac{d_w}{2}(F_{yfl} - F_{yfr}) \sin \delta \tag{3}$$

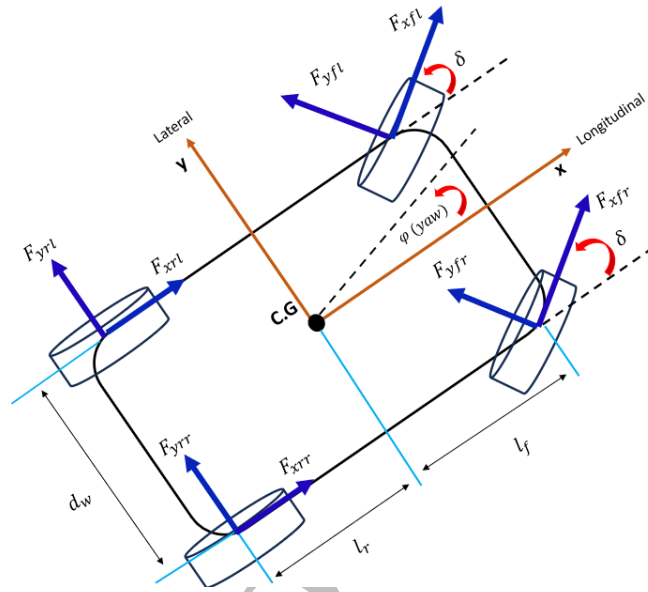


Figure 1. Force vector of nonlinear vehicle model [2]

2.1.1 Nonlinear tire characteristic

Dugoff's tire model was used to determine nonlinear tire characteristics. Eq. 4 expresses the tire slip ratio (ρ_{ij}), which can be determined by computing the difference between tire angular velocity, V_w with vehicle's longitudinal velocity, V_x and divided by vehicle's longitudinal velocity. Setting the slip ratio to an absolute value is crucial, as it ensures that the tire's slip ratio remains within the optimal limits of the tire-road friction coefficient, enhancing performance across a range of driving conditions. When a vehicle corners, its inner tire experiences a reduction in velocity compared to the vehicle's overall speed, leading to a negative slip ratio. Here, the integral i reflects the relationship between the front and rear tires, while j represents the dynamics of the right and left tires. Understanding these factors is essential for optimizing vehicle handling and safety.

$$\rho_{ij} = \left| \frac{V_{wij} - V_x}{V_x} \right| \tag{4}$$

Eq.s 5, 6, 7, and 8 provide vital insights into the dynamics of vehicle performance by detailing the sideslip angle for both the front and rear tires [2]. Those equations also illustrate how the velocity vectors of these tires relate to the vehicle's longitudinal axis, offering a clear understanding of how these factors influence handling and stability on the road. These angles are represented as $\alpha_f, \alpha_r, \theta_{vf},$ and θ_{vr} [2].

$$\alpha_f = \delta - \theta_{vf} \tag{5}$$

$$\alpha_r = -\theta_{vf} \tag{6}$$

$$\theta_{vf} = \tan^{-1} \left(\frac{V_y + l_f \dot{\phi}}{V_x} \right) \tag{7}$$

$$\theta_{vr} = \tan^{-1} \left(\frac{V_y - l_r \dot{\phi}}{V_x} \right) \tag{8}$$

Eq.s 9 and 10 show the longitudinal and lateral force equation.

$$F_{xij} = C_{\sigma} \frac{\rho_{ij}}{1 + \rho_{ij}} f(\lambda) \tag{9}$$

$$F_{yij} = C_{\alpha} \frac{\tan \alpha}{1 + \rho_{ij}} f(\lambda) \tag{10}$$

For front tires, a specific equation applies, while rear tires follow a different formula where α equals α_f and α equals α_r respectively. Additionally, λ is calculated using Eq. 11, with the function's conditions, $f(\lambda)$ outlined in Eq.s 12 and 13.

$$\lambda = \frac{\mu F_z (1 + \rho_{ij})}{2 [(C_{\sigma} \rho_{ij})^2 + (C_{\alpha} \tan(\alpha))^2]^{1/2}} f(\lambda) \tag{11}$$

$$f(\lambda) = (2 - \lambda)\lambda \quad \text{if } \lambda < 1 \tag{12}$$

$$f(\lambda) = 1 \quad \text{if } \lambda > 1 \tag{13}$$

In the context of tire performance, F_z is the vertical force resulting from load transfer on the tire, while μ stands for the tire-road friction coefficient [2]. As shown in Eq. 14, μ_{ij} is specified for each tire, using a dry road surface constant, k , fixed at 0.9.

$$\mu_{ij} = -1.05k[\exp(-45\rho_{ij}) - \exp(-0.45\rho_{ij})] \tag{14}$$

Next, the tire dynamic model is expressed in Eq.s 15, 16, and 17. The tire's traction torque, driving torque, and inertia are represented by the letters T_f , T_d , and I_{tire} , respectively. As shown in Eq. 15, the tire's angular acceleration is calculated by subtracting the friction torque from the driving torque and dividing the result by the tire's inertia.

$$\frac{T_d - T_f}{I_{tire}} = \frac{d\omega}{dt} \tag{15}$$

Eq. 16 calculates a tire's angular velocity through integrating its rotational acceleration over the course of time [24]. Eq. 17 calculates the tire's linear velocity by multiplying the angular velocity with the tire's radius, ensuring accurate performance assessment [24].

$$\int \frac{d\omega}{dt} = \omega \tag{16}$$

$$V_t = r_{tire}\omega \tag{17}$$

2.1.2 Load Transfer Model

The load transfer model was used to calculate vertical forces at each tire [16]. This model considers both longitudinal and lateral load transfers, as detailed in Eq.s 18 to 21. It requires the longitudinal and lateral vehicle accelerations, denoted as a_x and a_y . The model consists of three key components: lateral load transfer, longitudinal load transfer, and static force, all crucial for optimizing vehicle performance. The vehicle's static force is increased by the additional load that is placed on it. Every tire's static mass, m_{ij} was considered in this investigation. A specific set of loads labelled as $load_{ij}$ was strategically applied to each tire to effectively simulate an imbalanced overloading scenario. The parameters h_{cg} and g are the height from the vehicle's CG and the gravitational force, accordingly [2].

$$F_{zfr} = (m_{fr} + load_{ij})g \frac{l_r}{l} + \frac{m a_y h_{cg}}{d_w} - m a_x \frac{h_{cg}}{l} \tag{18}$$

$$F_{zfl} = (m_{fl} + load_{ij})g \frac{l_r}{l} - \frac{m a_y h_{cg}}{d_w} - m a_x \frac{h_{cg}}{l} \tag{19}$$

$$F_{zrr} = (m_{rr} + load_{ij})g \frac{l_f}{l} + \frac{m a_y h_{cg}}{d_w} + m a_x \frac{h_{cg}}{l} \tag{20}$$

$$F_{zrl} = (m_{rl} + load_{ij})g \frac{l_f}{l} - \frac{m a_y h_{cg}}{d_w} + m a_x \frac{h_{cg}}{l} \tag{21}$$

2.1.3 Kinematic Model

Kinematic modelling is an essential technique for effectively capturing a vehicle's motion through mathematical representation, independent of the forces acting upon it. This method relies solely on the geometric relationships within the system, ensuring precise and consistent mathematical equations. In this context, Eq.s 24 and 25 articulate the vehicle's

longitudinal, X and lateral, Y movements within an inertial coordinate frame. Similarly, Eq.s 22 and 23 focus on the respective longitudinal and lateral velocities, represented as \dot{X} and \dot{Y} .

$$\dot{X} = \dot{x} \cos \varphi - \dot{y} \sin \varphi \tag{22}$$

$$\dot{Y} = \dot{x} \sin \varphi + \dot{y} \cos \varphi \tag{23}$$

$$X(t) = \int_0^t \dot{X}(t) dt \tag{24}$$

$$Y(t) = \int_0^t \dot{Y}(t) dt \tag{25}$$

2.2 Collision Avoidance Scenario

Figure 2 shows a collision avoidance scenario with one stationary barrier and a straight path with multiple lanes. The obstacle width is denoted by W_v , while the road width is denoted by W_L . The length of the obstacle is directly linked to L_v . The optimal results in the CA scenario were obtained using the parameter values outlined in Table 1. In this experiment, the cone served as a crucial obstacle and is depicted as a yellow circle in Figure 2. This visualization is essential for understanding the experiment’s dynamics.

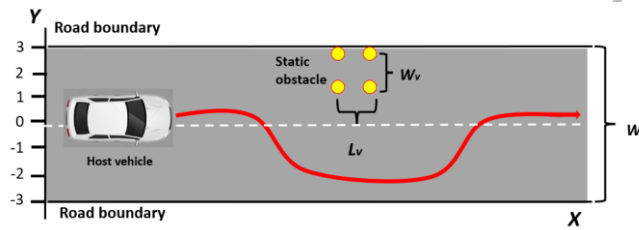


Figure 2. Vehicle’s maneuvering situation

Table 1. Parameters for CA experiment

Label	Parameter	Value
W_v	Obstacle width (m)	1.5
W_L	Road width (m)	6.0
L_v	Obstacle length (m)	4.0

The experiment was run on a dry road pavement and the vehicle behavior when avoiding an impediment is shown in Figure 2. Proton Persona, a sedan with a 1.6-liter engine and manual gearbox, was the vehicle utilized in this study [25]. The specifications of the test vehicle are displayed in Table 2. When the driver kept the speed at 30 km/h, the passenger in the back seat started to gather data. As the vehicle moved closer to the obstruction, the driver began to steer. Before being entered into the Data Acquisition Software (DAS), every piece of information was checked by the operator. The trial was carried out five times to ensure consistency. After that, the raw data were filtered and denoised using MATLAB software. This process was repeated as the vehicle navigated around obstacles at speeds of 30, 40, and 50 km/h. The velocity and steer tire angle data collected during these experiments were utilized to develop a reference generator for the CA simulation.

2.2.1 Simulation setup

The simulation was crafted using MATLAB Simulink. The reference generator produced reference signal data for steer tire angles and vehicle velocity as input data for the nonlinear vehicle modelling in MATLAB Simulink [2]. The influence of additional loads on both the left and right sides, acting as disturbances, was critically analyzed to showcase their significant impact on a vehicle’s trajectory while navigating around obstacles. Table 2 presents the essential vehicle modelling parameters that support this analysis.

Table 2. Vehicle modelling parameter [26]

Details	Symbol	Value	SI unit
Vehicle mass	m	1447.500	kg
Distance from the center of gravity towards the front part	l_f	1.080	m
Distance from the center of gravity towards the rear part	l_r	1.520	m
Centre gravity’s height	h_{cg}	0.479	m
Tire radius	r_{tire}	0.297	m

Table 3 displays the static mass of each tire, and Table 4 displays the value of the additional load applied to the left and right sides of the vehicle.

Table 3. Static mass of each tire

Label	Parameters	Value (kg)
m_{fr}	Tire's static mass on the front right	423.12
m_{fl}	Tire's static mass on the front left	423.12
m_{rr}	Tire's static mass on the rear right	300.63
m_{rl}	Tire's static mass on the rear left	300.63

Table 4. Load distribution on the front and rear side of the vehicle

Percentage (%)	Overall load (kg)	Right and left loads at the front (kg)	Right and left loads at the rear (kg)
10	144.75	72.38	72.38
20	289.50	144.75	144.75
30	434.25	217.13	217.13
40	579.00	289.50	289.50

The simulation was run at three different speeds corresponding to the CA experiment, effectively assessing the impact of added loads, $load_{ij}$ on the vehicle's dynamics. Load levels of 10%, 20%, 30%, and 40% were applied to the right side, both at the front and rear sections, as defined in Eqs 18 to 21. This systematic approach was replicated for the left side, ensuring thorough analysis and robust results. Figure 3 shows the CA block architecture for the vehicle model and the integrated controller for disturbance rejection (IC-DR) path tracking system that consists of longitudinal and lateral controller as well as reference trajectory for CA scenarios. However, this study only focuses on rejecting external disturbance, which is additional load distribution at each tire while avoiding obstacle.

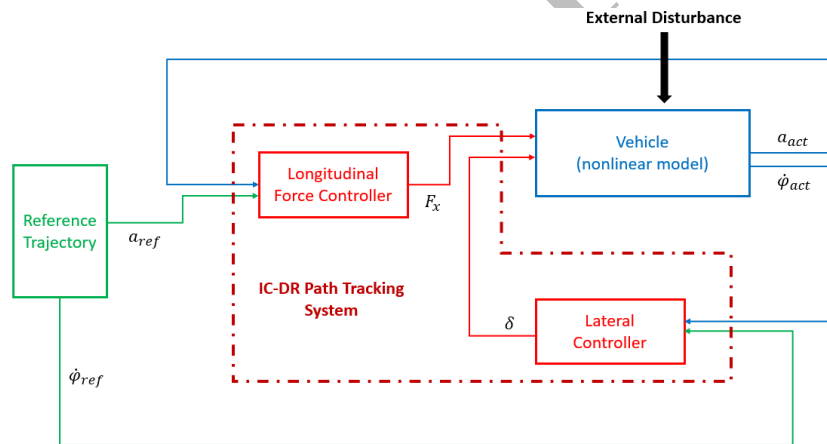


Figure 3. Collision avoidance system block diagram in simulation

2.3 Longitudinal Force Controller Design

Longitudinal controller is used to dictate the movement of nonlinear vehicle system in longitudinal direction. Eq. 26 expresses the simplified longitudinal actuator force, F_{ax} that acts at the center of the vehicle body that was used for the formulation of the longitudinal controller. Eq. 26 does not consider the rolling resistance effect of vehicle tires. The steer tire angle, δ in Eq. 26, was obtained from the output from the lateral controller as expressed in Eq. 54.

$$F_{ax} = ma_{des} - F_{yf} \sin \delta \tag{26}$$

The vehicle's mass and desired acceleration can be denoted as m and a_{des} . a_{error} is the difference between reference acceleration, a_{ref} and vehicle's actual acceleration, a_{act} that can be calculated using Eq. 27. F_{yf} is the lateral force that occurs at the center of the front tire in 2-tire modelling due to the presence of evasive steer tire angle, δ while avoiding an obstacle. The proportional derivative controller (PD) is used for vehicles to track reference acceleration, a_{ref} . Eq. 28 shows the PD controller formulation. The proportional gain, K_p and derivative gain, K_d were set to 30 and 500, respectively. The huge value of derivative gain will enhance the PD capabilities to track reference acceleration, which is in oscillation pattern as shown in Figures 6, 7 and 8 for 30, 40, and 50 km/h respectively, in Subsection 6.1.1.

$$a_{error} = a_{ref} - a_{act} \tag{27}$$

$$a_{des} = K_p a_{error} + K_d \frac{\Delta a_{error}}{\Delta t} \tag{28}$$

2.3.1 Force distribution

Eqs 29 and 30 express the force that is distributed at front, F_{axf} and rear, F_{axr} respectively. The length proportion between the front and rear centers of gravity determines how much force is transferred to the vehicle’s front and back sections.

$$F_{axf} = F_{ax} \frac{l_r}{l_f + l_r} \tag{29}$$

$$F_{axr} = F_{ax} \frac{l_f}{l_f + l_r} \tag{30}$$

Figure 4 illustrates how the longitudinal force, F_{ax} that acts on the center of the body is distributed at each tire accordingly. The force at the front and rear parts of the vehicle is divided by two, respecting to the right and left tire.

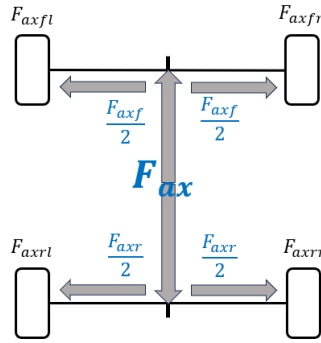


Figure 4. Longitudinal force distribution

The torque driving for each tire can be calculated as the product of the longitudinal force at each tire and the radius of the tire that corresponds to the front and rear part of the vehicle. The torque driving at each tire is written in Eq. 31, with component i representing front and rear and component j for right and left. The torque driving acts as an input to the nonlinear vehicle model as expressed in Eq. 15.

$$T_{dij} = F_{axij} \times r_{tire} \tag{31}$$

2.4 Optimal Lateral Controller Design

Due to the yaw rotational speed connection with the velocity components as stated in the dynamic equation of motion (Eq.s 1 and 2), a linear feedback control cannot be applied directly to a nonlinear system. As an option, the estimator in lateral controller, which is a Kalman state estimator, uses a linearized dynamic model to converge the measured state feedback value in estimator approximately to the desired state from reference trajectory for nonlinear vehicle model. The ensuing sections provide a detailed explanation of each model in the modeling block as shown in Figure 5 [20].

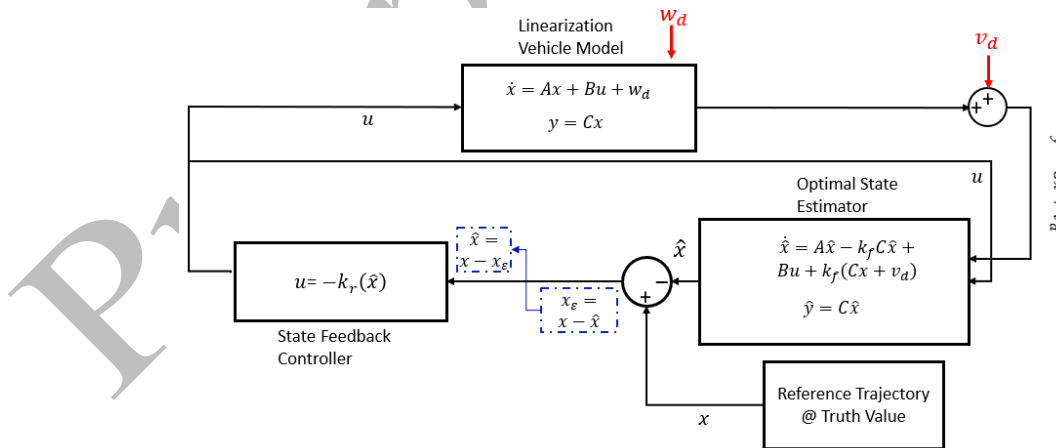


Figure 5. Lateral controller framework

2.4.1 Model linearization

The relationship between the tires and the pavement can be limited to the centers of the tire axis and represented by linear equations, assuming that the vehicle has zero acceleration along the trajectory. Several stages of simplification and assumption can be taken from Eq.s 1 and 2 to get a linear model of the vehicle’s dynamics. It should be emphasized that linearity does not cause any differences in the properties of the left and right tires; as a result, the equations provide a two-tire model. Linear dynamics of lateral velocity and yaw rotational velocity can be expressed in Eq.s 32 and 33, respectively.

$$m(\ddot{y} + V_x \dot{\phi}) = F_{yf} + F_{yr} \quad (32)$$

$$I_z \ddot{\phi} = l_f F_{yf} - l_r F_{yr} \quad (33)$$

It begins by assuming small side-slip angles for the tires and steering [27]. Eq.s 34 and 35 show the simplification of side-slip angles for front and rear tires, respectively.

$$\alpha_f = \delta - \left(\frac{V_y + l_f \dot{\phi}}{V_x} \right) \quad (34)$$

$$\alpha_r = - \left(\frac{V_y - l_r \dot{\phi}}{V_x} \right) \quad (35)$$

A tire lateral force model is involved in the second assumption. As a result of the lateral force being inside the linear range due to the minimal side-slip angles and can be simplified in Eq. 36 [27]. Eq.s 34 and 35 are substituted into Eq. 36 for front and rear lateral force, respectively.

$$F_y = C_\alpha \alpha \quad (36)$$

Then, the lateral force for front and rear tires in Eq. 36 can be substituted into linear dynamic equation of motion (Eq. 32) and yaw rotational velocity (Eq. 33), respectively. Eq. 37 presents the linearized model in state space equation including the disturbance, w_d .

$$\begin{aligned} \dot{x} &= Ax + Bu + w_d \\ y &= Cx \end{aligned} \quad (37)$$

where, the vehicle state is indicated as $x = [\dot{y} \ \dot{\phi}]^T$, respectively representing lateral velocity and yaw rate. The control input represents the steering angle of the front wheels $u = \delta$, and the output matrices is denoted as $C = [0 \ 1]$, the coefficient matrices are correspondingly denoted as

$$\begin{aligned} A &= \begin{bmatrix} a & b \\ c & d \end{bmatrix}, \\ &= \begin{bmatrix} \frac{-2(C_{\alpha f} - C_{\alpha r})}{mv_x} & -v_x - \frac{2(C_{\alpha f} l_f - C_{\alpha r} l_r)}{mv_x} \\ -\frac{2(l_f C_{\alpha f} - l_r C_{\alpha r})}{I_z v_x} & -\frac{2(l_f^2 C_{\alpha f} + l_r^2 C_{\alpha r})}{I_z v_x} \end{bmatrix}, \\ B &= \begin{bmatrix} e \\ f \end{bmatrix}, \\ &= \begin{bmatrix} \frac{2 C_{\alpha f}}{m} \\ \frac{2 l_f C_{\alpha f}}{I_z} \end{bmatrix} \end{aligned}$$

2.4.2 Kalman state estimator design

Kalman state estimator uses the linearized model as an internal model to generate a reliable state vector for the regulator to compute feasible input to nonlinear vehicle model [14]. Eq. 38 shows the derivation of the Kalman state estimator in state space equation. The variables \hat{x} , k_f , and \hat{y} stand for estimator state, estimator gain, and output from state estimator, respectively. The final form of state space equation for Kalman state estimator is expressed in Eq. 39.

$$\begin{aligned} \dot{\hat{x}} &= A\hat{x} + Bu + k_f(y - \hat{y}) \\ &= A\hat{x} + Bu + k_f[(Cx + v_d) - C\hat{x}] \end{aligned} \quad (38)$$

$$\begin{aligned} \dot{\hat{x}} &= (A - k_f C)\hat{x} + Bu + k_f(Cx + v_d) \\ \hat{y} &= C\hat{x} \end{aligned} \quad (39)$$

To make sure the state in estimator resembles the state from reference trajectory (nonlinear model), the error between both states must be converged to approximately zero. Eq.s 40 and 41 show the error between both states, x_ε and error between both states over time, \dot{x}_ε respectively.

$$x_\varepsilon = x - \hat{x} \quad (40)$$

$$\dot{x}_\varepsilon = \dot{x} - \dot{\hat{x}} \quad (41)$$

Eq.s 42 to 45 express the derivation of Eq. 41.

$$\dot{x}_\varepsilon = Ax + Bu + w_d - [A\hat{x} - k_f C\hat{x} + Bu + k_f(Cx + v_d)] \quad (42)$$

$$\dot{x}_\varepsilon = Ax + Bu + w_d - A\hat{x} + k_f C\hat{x} - Bu - k_f(Cx + v_d) \quad (43)$$

$$\dot{x}_\varepsilon = Ax + w_d - A\hat{x} + k_f C\hat{x} - k_f Cx - k_f v_d \quad (44)$$

$$\dot{x}_\varepsilon = (A - k_f C)(x - \hat{x}) + w_d - k_f v_d \quad (45)$$

By substituting Eq. 41 into Eq. 45, the final equation is expressed as Eq. 46.

$$\dot{x}_\varepsilon = \dot{x}_\varepsilon = (A - k_f C)(x_\varepsilon) + w_d - k_f v_d \quad (46)$$

Kalman estimator gain, k_f is used to converge the error between the estimator state with reference trajectory generator state in presence of disturbance weightage, w_d and noise weightage, v_d . Eq. 47 presents the linear quadratic estimator for ideal state, J_k concerning the subsequent cost function. The impacts of noise and disturbance are explicitly included in this cost function, which is necessary to find the ideal ratio between noise attenuation and disturbance estimation.

$$J_k = \lim_{t \rightarrow \infty} E \left((x(t) - \hat{x}(t))(x(t) - \hat{x}(t))^T \right) \quad (47)$$

Eq. 48 shows the matrices for weightage of disturbance and sensor noise. However, in this study, the noise attenuation weightage was approximated to zero, $v_d \approx 0$. This is because this study only focuses on rejecting external disturbance. The Kalman state estimator only focuses on rejecting the disturbance at yaw rate as the nonlinear vehicle model only measured the output of vehicle's yaw rate.

$$w_d = \begin{bmatrix} \sigma_y^2 = 0.001 & 0 \\ 0 & \sigma_\phi^2 = 1 \end{bmatrix}, \quad v_d = 0.001 \quad (48)$$

The algebraic Riccati equation (ARE) is used to generate Kalman estimator gain, k_f from cost function equation, where Y is the solution generated from ARE as expressed in Eq. 49. Matrices A and C are acquired from the linear dynamic model, while w_d and v_d are the matrix covariances of the disturbance and noise corresponding to state in linear model and measured state output, respectively. The w_d and v_d matrix covariance must be in positive semi-definite and positive definite to make sure the optimal state estimator gain, k_f that has been produced can stabilize the state by following reference state.

$$YA^T + AY - YC^T v_d^{-1} CY + w_d = 0 \quad (49)$$

Eq. 50 shows the formulation of the Kalman estimator gain, k_f [28].

$$k_f = YC^T v_d^{-1} \quad (50)$$

2.4.3 State feedback regulator design

The regulator has been designed to produce a feasible regulator gain, k_r corresponding to the error between the state generated by Kalman estimator with the state truth value. Here, the state truth value refers to the optimized reference yaw rate from the reference generator. The ideal state of the vehicle, excluding the impact of external disturbances or sensor noise, is known as the state truth or reference state. The states in the linearized model and the state truth are regarded as x for the derivation. Eq.s 51 to 53 express the derivation of the state feedback controller where $\hat{x} = x - x_\varepsilon$ [20].

$$\dot{x} = Ax - Bk_r \hat{x} + w_d \quad (51)$$

$$\dot{x} = Ax - Bk_r(x - x_\varepsilon) + w_d \quad (52)$$

$$\dot{x} = (A - Bk_r)x + Bk_r x_\varepsilon + w_d \quad (53)$$

Eq. 54 shows the state feedback control strategy. The lateral controller output, u can be denoted as steer tire angle, δ input to the nonlinear vehicle system.

$$u = -k_r(\hat{x}) \quad (54)$$

The quadratic cost function is used to determine feasible gain, k_r by setting the ratio of the state error, Q and control gain actuator, R . Eq. 55 shows the linear quadratic regulator, J_r formulation.

$$J_r = \sum_{t=0}^{t=\infty} (\hat{x})^T Q (\hat{x}) + u^T R u \quad (55)$$

Eq. 56 expresses the weighting parameters of state feedback controller, Q and control weighting effort, R . The control weighting effort was set to 0.001. It is because the reference signal only performs in linear operating point, which indicates the control effort that yield steer wheel angle only operates within actuator capabilities. The weighting for state feedback controller only emphasizes minimizing the error between the yaw rate from reference generator and the yaw rate of the vehicle. The Q and R weighting parameters must be in positive semi-definite and positive definite, respectively.

$$Q = \begin{bmatrix} Q(\dot{y}) = 0.001 & 0 \\ 0 & Q(\phi) = 1 \end{bmatrix}, \quad R = 0.001 \quad (56)$$

The solution for the ARE, which is P , is calculated using Eq. 57. Then, this P value is used to calculate the regulator gain, k_r . Then, the feasible regulator gain is generated as shown in Eq. 58 [28]. Matrices A and B are obtained from the linear dynamics model.

$$PA + AP^T - PBR^{-1}B^T P + Q = 0 \tag{57}$$

$$k_r = PB^T R^{-1} \tag{58}$$

3. Results and Discussion

This section discusses the proposed control technique for disturbance rejection while avoiding an obstacle at 30, 40, and 50 km/h in simulation environment. Section 6.1 focuses on the analysis of IC-DR path tracking system performance. Section 6.2 shows the effect of applying IC-DR into the vehicle system.

3.1 Analysis of IC-DR Path Tracking Performance

Figures 6, 7, and 8 show the longitudinal controller performance where the reference acceleration is represented by the bold blue dotted line. The acceleration of the vehicle as 10% load was added to the right and left parts of the tire is represented by red and yellow lines respectively, while the acceleration for 20% load at the right and left parts of the tire is represented by purple and light green lines, respectively. The sky blue and pink lines represent the acceleration of the vehicle when 30% of the load was added at the right and left parts of the tire accordingly. Finally, the blue and orange lines represent acceleration of the vehicle when 40% load was added at the right and left tires, correspondingly. Each line color for 10%, 20%, 30%, and 40% for the right and left parts of the tire were set to be the same for velocity of 30, 40, and 50 km/h.

Figures 9, 10, and 11 illustrate the lateral controller performance where the reference yaw rate is denoted as bold blue dotted line. The yaw rate of the vehicle as 10% load was added to the right and left parts of the tire is represented as red and yellow lines respectively, while the yaw rate for 20% load at the right and left parts of the tire is represented by purple and light green lines, respectively. The sky blue and pink lines represent the yaw rate of the vehicle when 30% of the load was added at the right and left parts of the tire, respectively. The blue and orange lines represent the yaw rate of the vehicle when 40% load was added at the right and left tires, correspondingly. Each line color for 10%, 20%, 30%, and 40% for the right and left parts of the tire were set to be same for the three velocities.

3.1.1 Longitudinal force controller

Figure 6 shows the changes of vehicle acceleration corresponding to the time of the vehicle travel for 30 km/h. The acceleration of the vehicle was maintained around -0.04 to -0.065 for reference and all additional loads at the right or left parts of the tire as the vehicle moved in straight trajectory from 0 to 3.5 s before starting to maneuver to avoid the obstacle. The vehicle's acceleration started to significantly change from 4 to 8 s due to the maneuver. As the vehicle surpassed the obstacle and started to enter the original lane, the acceleration for the reference and all additional loads at the right or left parts of the tire increased constantly from 8 to 10 s. This is because after the lane change, the change of lateral acceleration value directly affects the total vehicle body acceleration. To maintain the vehicle body speed, corresponding to reference speed, the driver must press or release the gas pedal and this directly affects the magnitude of vehicle body acceleration as shown in Figures 6, 7, and 8 for 30, 40, and 50 km/h, accordingly.

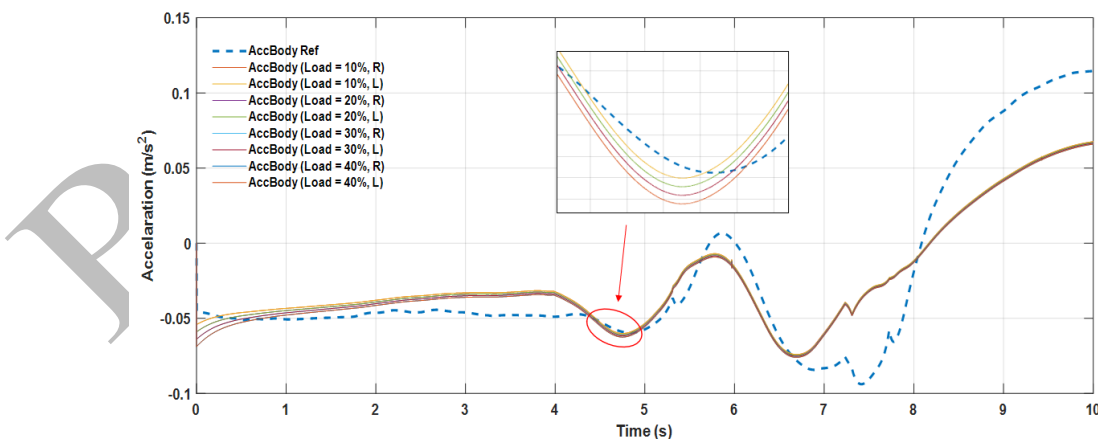


Figure 6. Longitudinal controller performance at 30 km/h

Figure 7 illustrates the acceleration of the vehicle for reference trajectory and all the load percentages at the right and left parts of the tire corresponding to the time of vehicle travel for 40 km/h. There is significant deceleration happening as the vehicle travelled from 0 to 2.5 s. As the vehicle started to maneuver to avoid an obstacle from 2.5 to 6.5 s, the acceleration of the vehicle varied from -0.015 to 0.039 m/s². When the vehicle passed the obstacle, it experienced constant deceleration from 0.039 to 0.018 m/s².

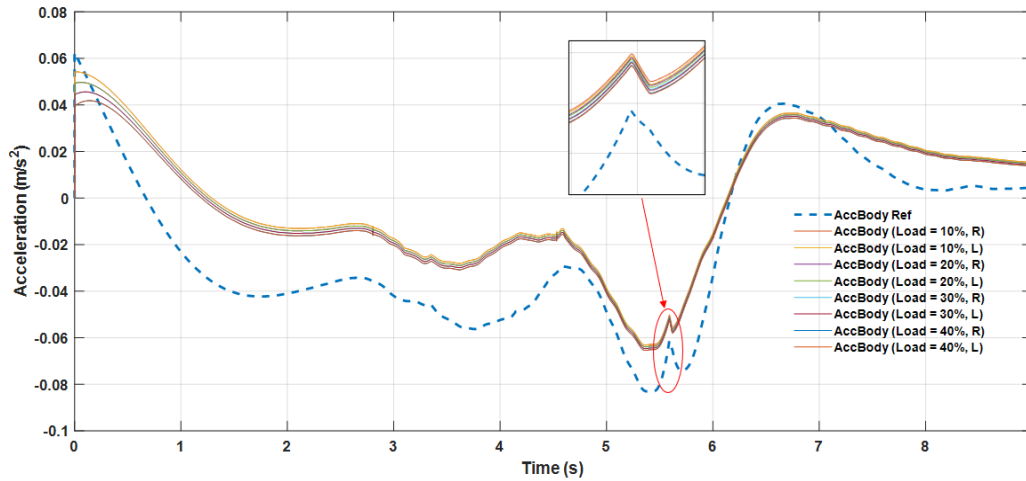


Figure 7. Longitudinal controller performance at 40 km/h

Figure 8 shows the acceleration of the vehicle for reference trajectory and all the load percentages at the right and left parts of the tire corresponding to the time of the vehicle travel for 50 km/h. Although the vehicle travelled in a straight trajectory, the acceleration slightly increased around 0.06 to -0.035 m/s^2 from 1 to 2 s after having maximum drop around 0.043 to -0.07 m/s^2 at 0 to 0.1 s. The vehicle’s acceleration for reference trajectory and all the percentages at the right and left parts of the tire varied from -0.061 to 0.016 m/s^2 corresponding to the time of the vehicle maneuver to avoid obstacle from 2 to 6.3 s. As the vehicle passed the obstacle, the acceleration maintained around 0.005 to 0.02 m/s^2 from 6.3 to 8 s.

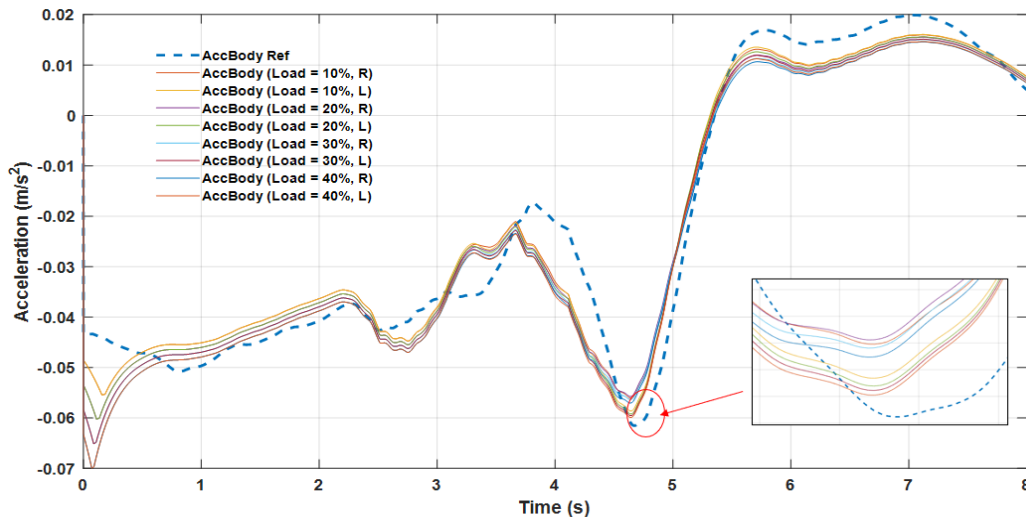


Figure 8. Longitudinal controller performance at 50 km/h

The vehicle’s acceleration significantly changed while avoiding an obstacle due to significant changes of the lateral acceleration of the vehicle body. This is because the changes of the steer tire angle at the front tire directly affect the lateral force at the front tire and consequently increase the total lateral force acting at the center of the vehicle body as expressed in Eq. 2. The relationship of total lateral force with lateral acceleration of the vehicle is directly proportional with each other. The lateral force can also be affected by the load transfer phenomena during vehicle maneuvering while avoiding an obstacle. Dugoff’s tire model expresses the relationship of lateral force with normal force as shown in Eq.s 10 and 11 which are directly proportional to each other. Tables 5 and 6 shows the mean square error (MSE) between reference acceleration of the vehicle with vehicle’s acceleration of all additional load percentages at three different velocities for the right and left parts of the tire, respectively.

Table 5. MSE of the vehicle’s acceleration for additional load on right part of the tire

Percentage (%)	Velocity = 30 km/h	Velocity = 40 km/h	Velocity = 50 km/h
10	0.000602	0.000433	2.28×10^{-5}
20	0.000600	0.000400	2.69×10^{-5}
30	0.000601	0.000369	3.13×10^{-5}
40	0.000604	0.000341	3.70×10^{-5}

When the velocity of the vehicle increases, the MSE value for tracking acceleration decreases. This is because the reference acceleration corresponds to the behaviors of the driver. The acceleration tracking error performs better when the vehicle travels at higher velocity while avoiding an obstacle compared to lower velocity.

Table 6. MSE of the vehicle’s acceleration for additional load on left part of the tire

Percentage (%)	Velocity = 30 km/h	Velocity = 40 km/h	Velocity = 50 km/h
10	0.000602	0.000432	2.26×10^{-5}
20	0.000600	0.000399	2.62×10^{-5}
30	0.000600	0.000369	3.08×10^{-5}
40	0.000604	0.000341	3.67×10^{-5}

3.1.2 Lateral controller

Figure 9 shows the yaw rate of the vehicle corresponding to the time of the vehicle travel for 30 km/h while avoiding obstacle. The yaw rate of the vehicle for the reference and all load percentages at the right and left parts of the tire maintained around 0 to 0.015 rad/s from the beginning of vehicle travel until 3.5 s. Then, the vehicle’s yaw rate started to vary around -0.15 to 0.2 rad/s corresponding to the time as the vehicle starts to maneuver at 3.5 s until the end of the trajectory.

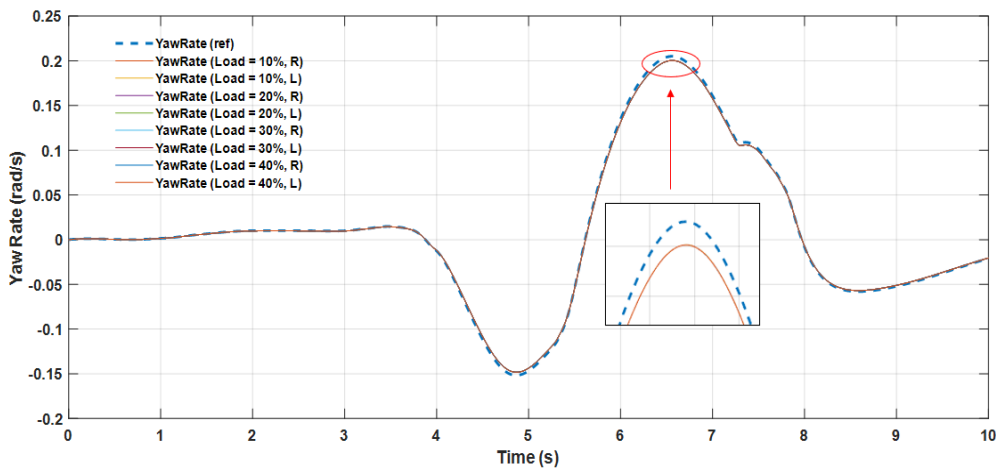


Figure 9. Lateral controller performance at 30 km/h

Figure 10 shows the lateral controller performance as the vehicle travelled at 40 km/h while avoiding obstacle. The yaw rate of the reference trajectory and all additional load percentages at the right and left parts of the tire started to show significant changes as the vehicle maneuvered while avoiding obstacle at 2.4 s until the end of the trajectory. The maximum yaw rate was recorded at around 0.16 rad/s while the minimum yaw rate was -0.08 rad/s (Figure 10).

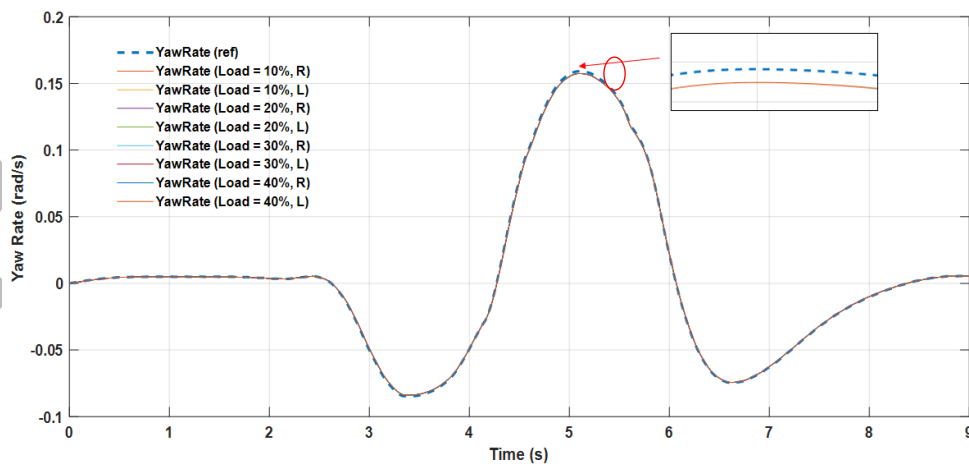


Figure 10. Lateral controller performance at 40 km/h

Figure 11 illustrates the vehicle’s yaw rate at 50 km/h. The vehicle showed a huge change in yaw rate value as it started to maneuver to avoid obstacle from 2 to 7 s for the reference trajectory and the trajectory for all additional load percentages at the right and left parts of the tire. The yaw rate for all additional load percentages for 50 km/h showed a slight variation as shown in red circle in Figure 11 compared to the yaw rate for all additional loads for 30 and 40 km/h as shown in Figures 9 and 10, respectively.

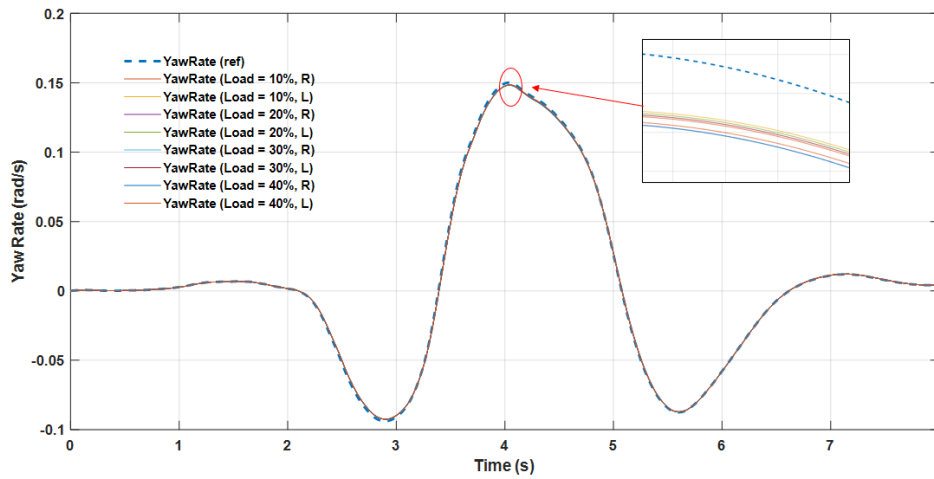


Figure 11. Lateral controller performance at 50 km/h

The vehicle’s yaw rate significantly changed while avoiding obstacle for all velocities due to the changes of the lateral force, which is directly proportional to the yaw rate of the vehicle as expressed in Eq. 3. The changes of lateral force were also affected by steer tire angle and normal force at each tire of the vehicle, especially during avoiding an obstacle with additional load on the right or left part of the tire. Without a decent lateral controller, the load transfer phenomenon will affect the yaw rate of the vehicle along the CA trajectory. The lateral controller reduced the error between vehicle’s yaw rate for reference trajectory and trajectory of all additional load percentages at the right and left parts of the tire for all speeds. Tables 7 and 8 show the mean square error (MSE) between the reference yaw rates and the yaw rate of all additional load percentages at three different velocities for the right and left parts of the tire, respectively.

Table 7. MSE of the vehicle’s yaw rate for additional load on right part of the tire

Percentage (%)	Velocity = 30 km/h	Velocity = 40 km/h	Velocity = 50 km/h
10	4.02733×10^{-6}	5.26905×10^{-7}	8.60068×10^{-7}
20	4.03568×10^{-6}	5.27893×10^{-7}	9.14103×10^{-7}
30	4.04405×10^{-6}	5.28883×10^{-7}	9.19096×10^{-7}
40	4.05245×10^{-6}	5.29876×10^{-7}	9.21130×10^{-7}

The yaw rate tracking error has excellent performance when the vehicle avoided obstacle at 40 km/h for both parts of tire. In terms of additional load percentage, the performance of yaw rate tracking error was much better at 10% for each vehicle velocity compared to other additional load percentages.

Table 8. MSE of the vehicle’s yaw rate for additional load on left part of the tire

Percentage (%)	Velocity = 30 km/h	Velocity = 40 km/h	Velocity = 50 km/h
10	4.01981×10^{-6}	5.21551×10^{-7}	7.68952×10^{-7}
20	4.03122×10^{-6}	5.24289×10^{-7}	7.75403×10^{-7}
30	4.04163×10^{-6}	5.26576×10^{-7}	7.87473×10^{-7}
40	4.05129×10^{-6}	5.28499×10^{-7}	8.0029×10^{-7}

3.2 Trajectory Analysis during Collision Avoidance Maneuverer

Figures 12–17 illustrate the trajectory of the vehicle on the effect of external disturbance while avoiding obstacle as the vehicle travelled at three different velocities. The reference trajectory is represented by dotted blue line, while the vehicle’s trajectory as the load was added to the right or left part of the tire is represented by red line in all figures. The integration of the IC-DR into vehicle CA system produced a feasible trajectory that can handle additional load disturbances, represented by orange line in all figures. The obstacle is illustrated as a yellow rectangle with red dotted line acting as boundary for the rectangle’s parameter.

3.2.1 Velocity = 30 km/h

Figure 12 shows the vehicle’s maneuvering at 30 km/h with different additional load percentages on the right part of the tire. Figures 12 (a) and (b) show that, without an IC-DR tracking system, the vehicle managed to avoid obstacle although it experienced a small oversteering effect along 50 to 70 m when the additional load was 20%. As additional load increased, the oversteering effect also increased while avoiding obstacle. Figure 12 (c) for additional load = 30% shows the slight oversteering effect between 50 and 70 m, which was higher compared to the trajectory with 20% additional load. The oversteering effect affected vehicle trajectory with 40% additional load added, where it slightly deviated from reference trajectory from 50 m until the end of trajectory. This shows that IC-DR tracking system integration into vehicle

CA system is necessary as it can reject additional load disturbance and prevent the vehicle from experiencing excessive understeering or oversteering while avoiding obstacles.

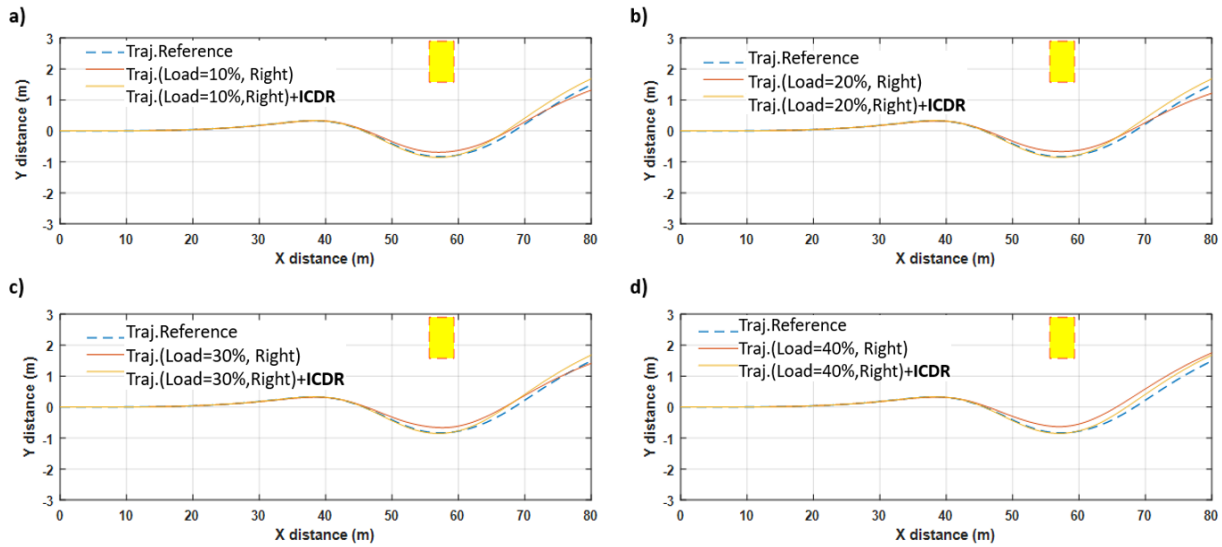


Figure 12. Vehicle maneuvering at 30 km/h corresponding to additional load on the right part of the tire: (a) 10%, (b) 20%, (c) 30%, and (d) 40%

Figure 13 shows the vehicle maneuvering at 30 km/h with additional load on the left part of the tire. The vehicle experienced an understeering effect when additional load increased to 10% and 20%. The effect was clearly visible along the trajectory as the vehicle passed the obstacle and started to enter the initial lane from 70 m until the end of the trajectory. The load transfer phenomena affected the trajectory of the vehicle as additional load increased from 10% to 40% by causing slight oversteering to the vehicle’s trajectory as shown in Figure 13, between 44 and 63 m. It underwent significant understeering until the end of the trajectory for 10% and 20% additional load. IC-DR tracking system integration into the CA system achieved a reduction in understeering for 20% additional load and significant oversteering effect for all additional load percentages.

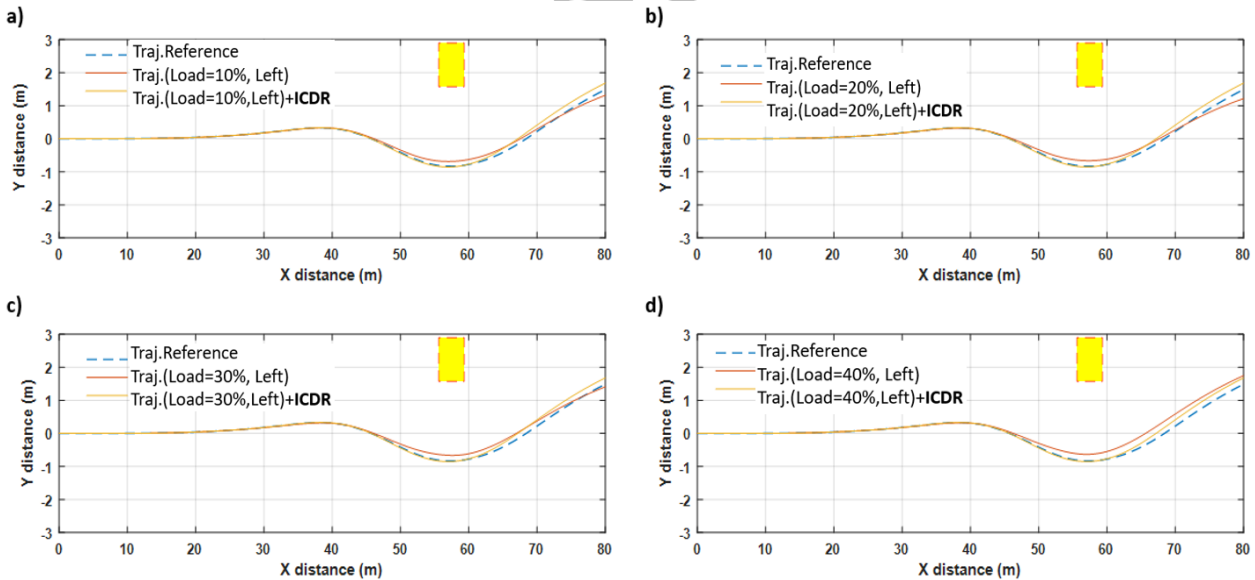


Figure 13. Vehicle maneuvering at 30 km/h corresponding to additional load on the left part of the tire: (a) 10%, (b) 20%, (c) 30%, and (d) 40%

3.2.2 Velocity = 40 km/h

Figure 14 shows the vehicle maneuverings at 40 km/h with additional load on the right part of the tire. The vehicle trajectory avoided obstacle without IC-DR tracking system for all loads. However, IC-DR tracking system is still essential when dealing with huge understeering problem for all additional load percentages while avoiding obstacle. Figures 14 (a) and (b) show that the vehicle experienced oversteering as soon as it exited the lane and started to experience understeering as it travelled for 67 and 64 m respectively. Figure 14 (c) shows that the vehicle experienced slight oversteering as soon as it exited the lane and started to experience huge understeering as the vehicle travelled for 60 m. The vehicle’s trajectory showed heavier understeering effect with 30% additional load compared to other percentages while avoiding obstacle, as

seen in Figure 14 (c). This effect can be seen when the vehicle is parallel with the obstacle at 60 m while avoiding obstacle until the end of the trajectory. The understeering effect is slightly reduced as additional load increased to 40% as shown in Figure 14 (d).

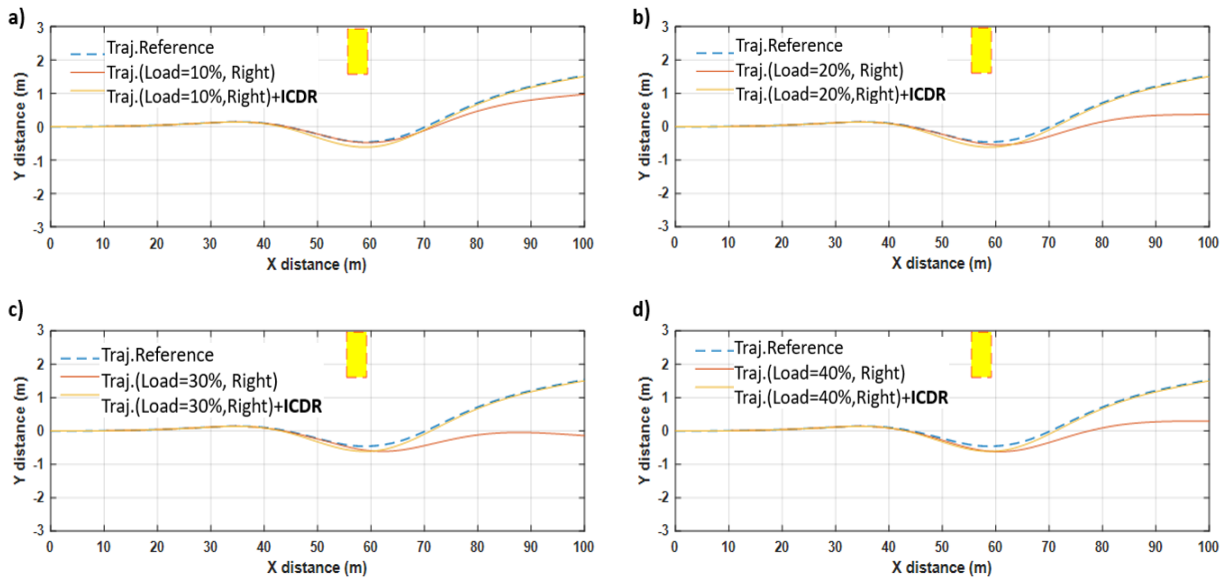


Figure 14. Vehicle maneuvering at 40 km/h corresponding to additional load on the right part of the tire: (a) 10%, (b) 20%, (c) 30%, and (d) 40%

Figure 15 shows the vehicle trajectory while avoiding obstacle at 40 km/h with additional load on the left part of the tire. The vehicle’s trajectory experienced understeering effect for additional load at all percentages on the left part of the tire. The understeering effect was significantly seen when additional load was 20% to 40%, with a huge understeering effect especially at 30%. This effect was initiated as the vehicle was surpassing the obstacle between 60 m until the end of the trajectory. Figure 15 (d) for 40% additional load shows a slightly lower understeering effect of vehicle trajectory compared to 30% additional load. Figure 15 (a) shows the lowest understeering effect on the vehicle’s trajectory with 10% additional load. IC-DR tracking system handled the error between the reference trajectories and the vehicle trajectory for all additional load percentages.

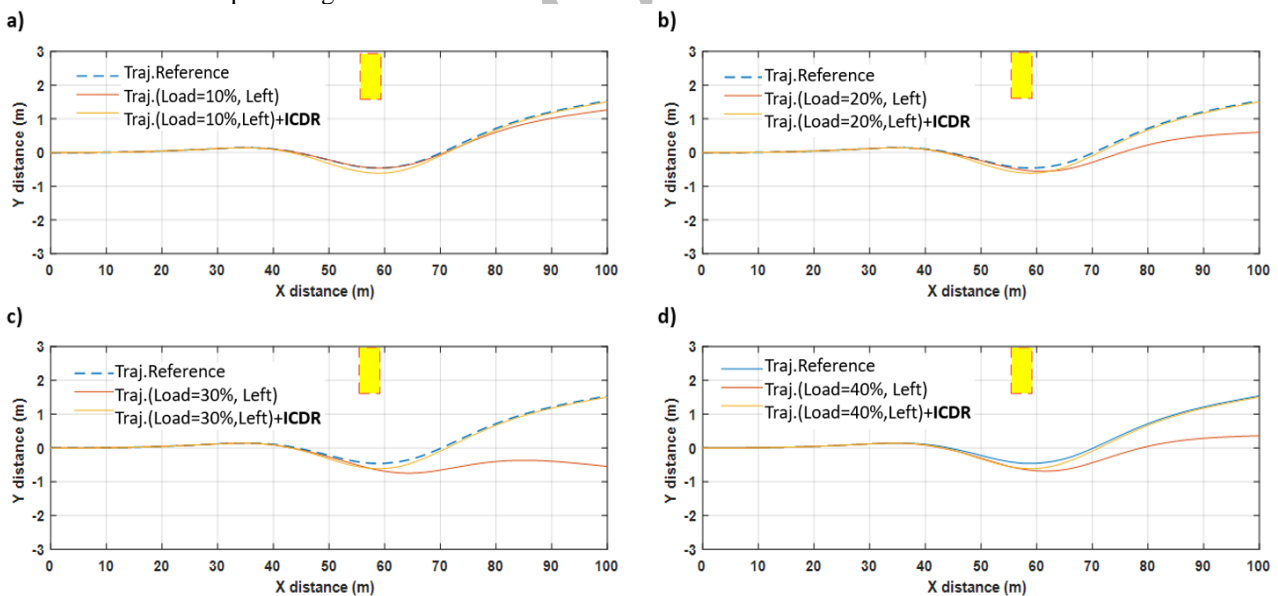


Figure 15. Vehicle maneuvering at 40 km/h corresponding to additional load on the left part of the tire: (a) 10%, (b) 20%, (c) 30%, and (d) 40%

3.2.3 Velocity = 50 km/h

Figure 16 shows the vehicle maneuverings at 50 km/h with additional load on the right part of the tire, illustrating the significant result of IC-DR tracking system integration into CA system. The vehicle’s trajectory started to deviate from reference trajectory and experienced understeering when avoiding obstacle at 45 m until the end of the trajectory for all additional load percentages.

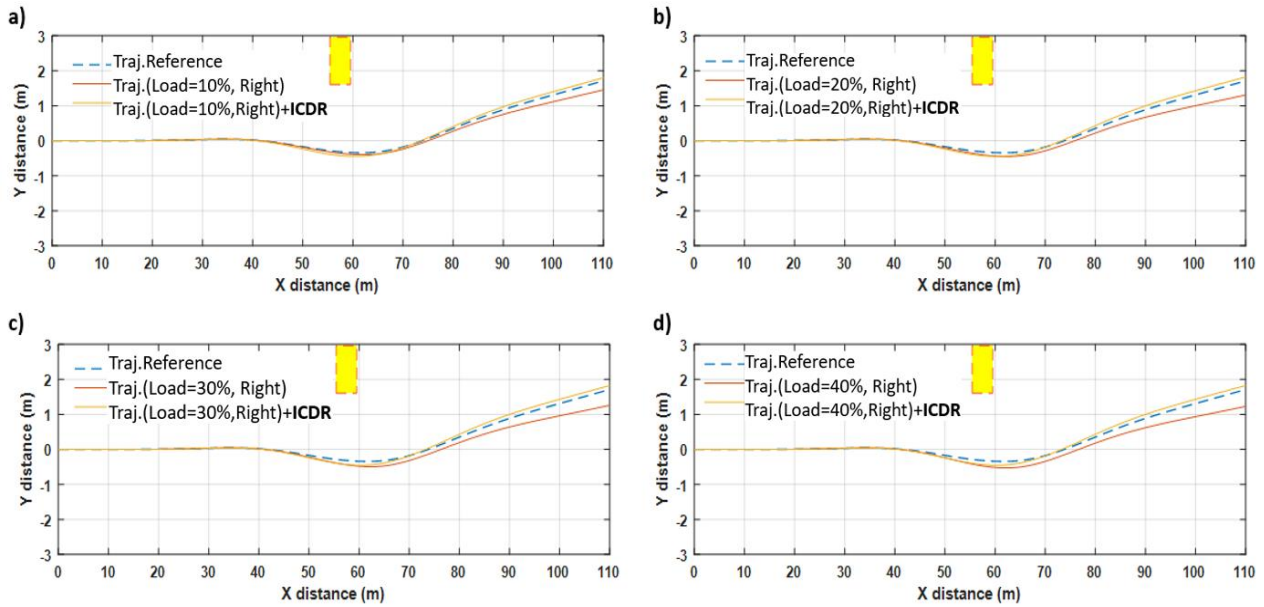


Figure 16. Vehicle maneuvering at 50 km/h corresponding to additional load on the right part of the tire: (a) 10%, (b) 20%, (c) 30%, and (d) 40%

Figure 17 shows the vehicle trajectory while avoiding obstacle at 50 km/h with additional load on the left part of the tire. As additional load increased, the understeering effect increased and ultimately resulted in a slight difference with reference trajectory. The vehicle managed to avoid obstacle without colliding with road barrier for all additional load percentages. The IC-DR path tracking system reduced the error between actual vehicle trajectory and reference path for all additional load percentages.

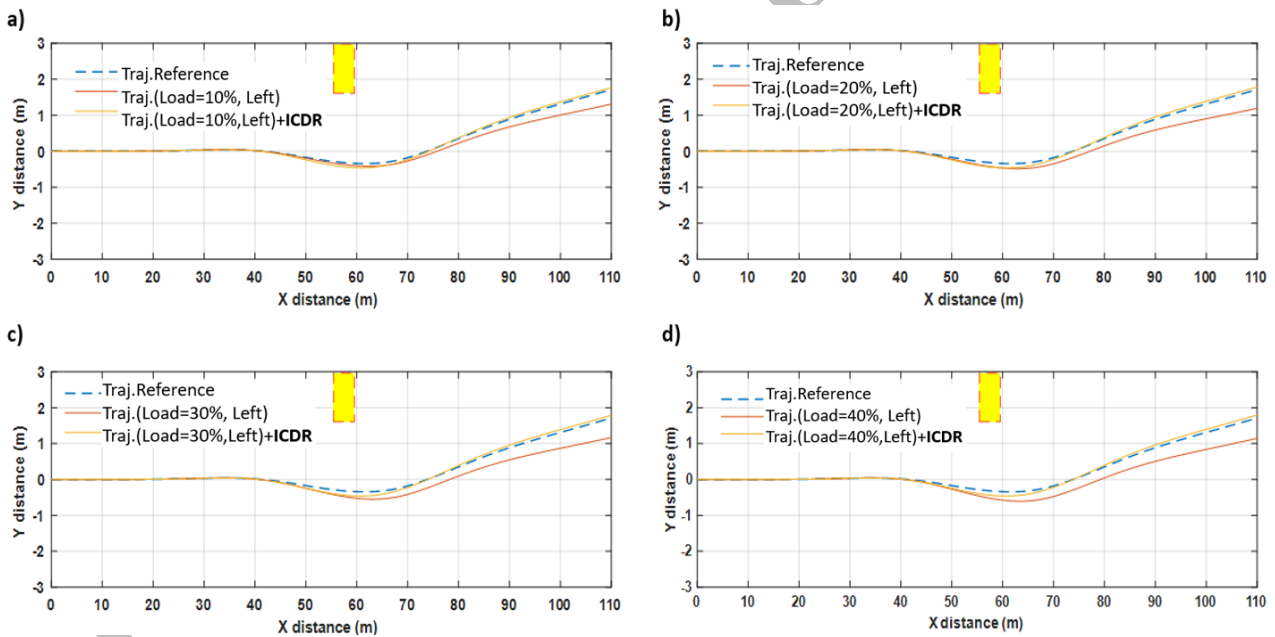


Figure 17. Vehicle trajectory while avoiding obstacle at 50 km/h corresponding to additional load on the left part of the tire: (a) 10%, (b) 20%, (c) 30%, and (d) 40%

3.2.4 Trajectory tracking error

Tables 9 and 10 present the MSE between the reference trajectory and the trajectory for additional load percentages on the right and left parts of the tire. The IC-DR tracking algorithm reduced the error between vehicle trajectory and reference trajectory with the existence of additional load disturbances. IC-DR tracking algorithm worked more efficiently at higher velocity (40 and 50 km/h) for all additional load percentages on the right and left parts of the tire. The IC-DR tracking algorithm performance is influenced by the reference trajectory produced by an experienced driver while avoiding obstacles. In another study [2], researchers have illustrated the reference trajectory pattern as it differs from each vehicle velocity. The driver tends to steer as early as possible when travelling at high velocity due to safety factors. Consequently, there is less maneuvering actuated by the driver when travelling at high velocity, which benefits IC-DR to track less aggressive maneuvering. The driver feels safer to steer a vehicle at smaller spacing headway (distance between vehicle

and obstacle) when at lower velocity. Consequently, this will produce aggressive maneuvering due to low attention to safety factors while avoiding obstacles [2].

Table 9. MSE of the vehicle’s trajectory for additional load on the right part of the tire

Percentage (%)	Velocity = 30 km/h	Velocity = 40 km/h	Velocity = 50 km/h
10	0.008446	0.003968	0.002811
20	0.008347	0.003967	0.003997
30	0.008249	0.003967	0.004147
40	0.008151	0.003968	0.004236

Table 10. MSE of the vehicle’s trajectory for additional load on the left part of the tire

Percentage (%)	Velocity = 30 km/h	Velocity = 40 km/h	Velocity = 50 km/h
10	0.008368	0.004067	0.002168
20	0.008301	0.004034	0.002548
30	0.008224	0.004010	0.002714
40	0.008140	0.003993	0.002879

3.3 Benchmark Tracking Controller

A comparison with the benchmark control system was made to demonstrate the advantages of the IC-DR in CA. The benchmark controller combined a lateral controller that employed a geometric-based approach (the Stanley method) and a longitudinal force controller to regulate feasible acceleration for the nonlinear vehicle dynamics as explained in Section 4.0. The Stanley method is the path tracking technique utilized by Stanford University’s autonomous vehicle in the DARPA Grand Challenge. The cross-track error, which is calculated from the front axle’s center to the closest point on the desired path, is the foundation of the Stanley method, a nonlinear control technique [29]. This approach generates an intuitive control rule by matching the control point with the steered front tires [29]. By fixing the orientation of the steering wheel to equal the heading inaccuracy, the first term of the control law guarantees that the wheels stay on the intended route [30]. This section focuses solely on comparing the IC-DR with a benchmark tracking controller in response to a 40% additional load distribution disturbance on the right part of the tire at different velocities. Figure 18 illustrates the comparison of the tracking system approach at 30, 40, and 50 km/h.

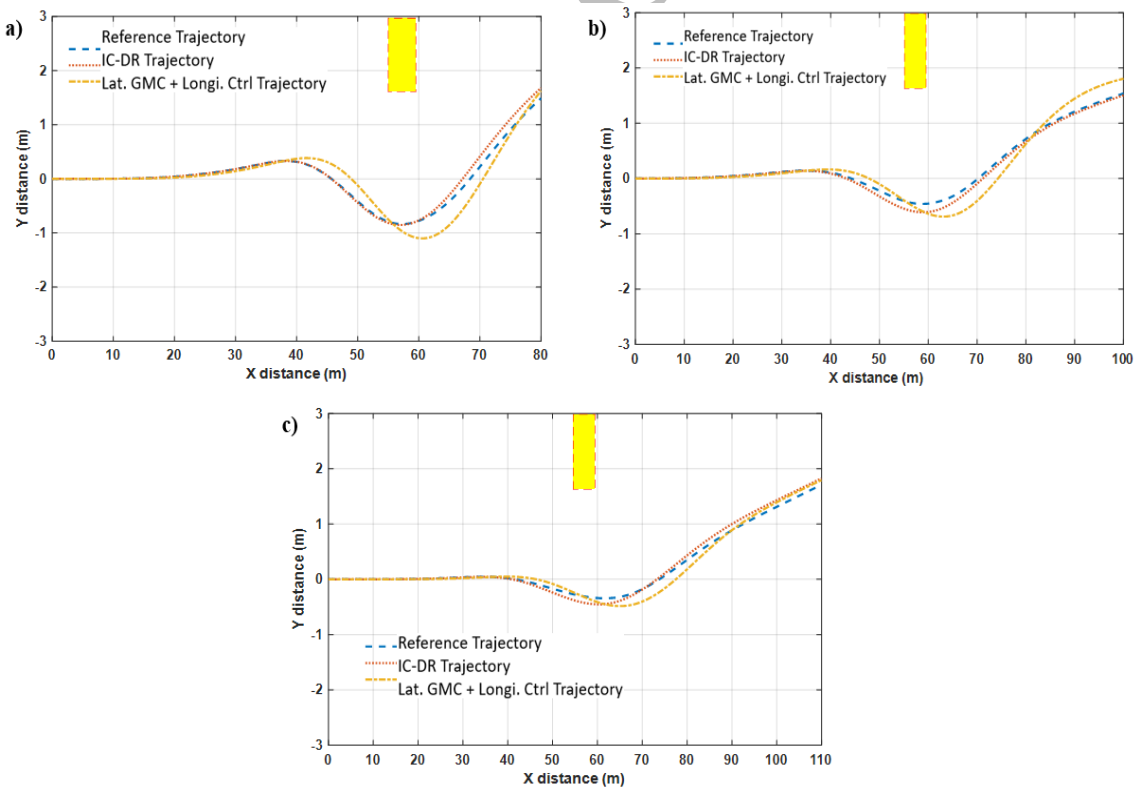


Figure 18. Collision avoidance trajectory comparison between IC-DR and benchmark tracking controller at (a) 30, (b) 40, and (c) 50 km/h.

There is a notable deviation in the trajectory of the benchmark control strategy, particularly when the vehicle exited the initial lane, maneuvered around an obstacle, and returned to the initial lane after avoiding a collision. This is in contrast to the IC-DR tracking system, which performed better across all tested speeds. Table 11 displays the MSE for each

tracking system strategy in relation to the reference trajectory. The results indicate that the IC-DR system surpasses the benchmark control strategy in tracking accuracy. The improvement in tracking capabilities for 30, 40, and 50 km/h are 77.50%, 86.67%, and 58.33%, respectively.

Table 11. Path tracking comparison with benchmark control strategy for vehicle's trajectory at 40% additional load at right tires

Path Tracking Controller	Trajectories MSE at 30km/h	Trajectories MSE at 40km/h	Trajectories MSE at 50km/h
ICDR	0.009	0.004	0.005
Lat. GMC + Longi. Controller	0.040	0.030	0.012

4. Conclusions

This paper presents the integrated controller for disturbance rejection (IC-DR) path tracking system implementation into collision avoidance (CA) system at different velocities: 30, 40, and 50 km/h. The CA system includes Dugoff's nonlinear tire characteristics for vehicle models to increase the reliability of the simulation platform. IC-DR tracking system is an integration of longitudinal force controllers with lateral controllers. The longitudinal force controller is essential for CA due to the necessity of tracking the changes of reference velocity during vehicle navigation at different velocities. The linear estimator model has been designed in a lateral controller for handling external disturbance presence while avoiding an obstacle. IC-DR tracking system is effective for vehicle navigation while avoiding obstacle, as presented in the simulation results. The results also prove the IC-DR tracking system's ability to strictly follow the reference trajectory as the deviation between actual vehicle models and reference signal is minimal. A significant low mean square error (MSE) was recorded across various performance metrics, such as acceleration, yaw rate, and vehicle trajectory. These results show the effectiveness of IC-DR in tracking the reference trajectory signal compared to benchmark control strategy across various percentages of load disturbance at different velocities. These findings show that the integration of estimator model for rejecting disturbance with control regulator becomes necessary when dealing with disturbances during the tracking of the reference signal. For future work, the IC-DR tracking system can be extended by applying a nonlinear control regulator and nonlinear estimator to increase its performance in different disturbance situations such as avoiding obstacles on slippery road. Next, the proposed control strategy technique has to be scalable when extended into real-time application by considering multiple obstacle avoidance as well as sensor signal delay into its formulation.

Declaration of Competing Interest

The authors affirm that they have no competing interests with regard to this work.

Acknowledgements

The author expresses gratitude to the Malaysian Ministry of Higher Education for offering a Fundamental Research Grant Scheme (FRGS/1/2022/TK10/UMP/02/27) (RDU220116). Special thanks to Autonomous Laboratory Universiti Malaysia Pahang Al-Sultan Abdullah for providing infrastructure needed to carry out this research.

Authorship Contribution Statement

Abdullah Zulkifli (Methodology; Writing-original draft; Conceptualization; Model Verification)

Mohamad Heerwan Peeie (Funding acquisition; Writing-review; Data Curation; Supervision)

M. Izhar Ishak (Writing-review; Data Curation; Supervision)

Muhammad Aizzat Zakaria (Writing-review; Visualization; Supervision)

References

- [1] M.C.J. Ying, W.K. Yew, P.J. Yew, A.Y. Her, "Real-time road accident reporting system with location detection using cloud-based data analytics," in *IECON 2022 – 48th Annual Conference of the IEEE Industrial Electronics Society*, 2022, pp. 1–6. <https://doi.org/10.1109/IECON49645.2022.9968507>
- [2] M.H. Peeie, A. Zulkifli, and M.I. Ishak, "Vehicle trajectory analysis on the effect of additional load distribution disturbance at different speeds for collision avoidance systems," *Automotive Experiences*, vol. 8, no. 1, 122-145, 2025. <https://doi.org/10.31603/ae.13200>
- [3] Y. Ma, Q. Liu, J. Fu, K. Liufu, Q. Li, "Collision-avoidance lane change control method for enhancing safety for connected vehicle platoon in mixed traffic environment," *Accident Analysis & Prevention*, vol. 184, p. 106999, 2023. <https://doi.org/10.1016/j.aap.2023.106999>
- [4] M. Wang, X. Chen, B. Jin, P. Lv, W. Wang, Y. Shen, "A Novel V2V Cooperative Collision Warning System Using UWB/DR for intelligent vehicles," *Sensors (Basel)*, vol. 21, 2021. [Online] Available: <https://api.semanticscholar.org/CorpusID:235229507>
- [5] L. Gonzalez, J.A. Matute-Peaspan, J.P. Rastelli, I. Calvo, "Longitudinal collision avoidance based on model predictive controllers and fuzzy inference systems," in *2020 IEEE 23rd International Conference on Intelligent Transportation Systems (ITSC)*, 2020, pp. 1–6. <https://doi.org/10.1109/ITSC45102.2020.9294584>

- [6] J. Liu, P. Jayakumar, J.L. Stein, T. Ersal, "Combined speed and steering control in high-speed autonomous ground vehicles for obstacle avoidance using model predictive control," *IEEE Transactions on Vehicular Technology*, vol. 66, no. 10, pp. 8746–8763, 2017. <https://doi.org/10.1109/TVT.2017.2707076>
- [7] S. Cheng, L. Li, H.-Q. Guo, Z.-G. Chen, P. Song, "Longitudinal collision avoidance and lateral stability adaptive control system based on MPC of autonomous vehicles," *IEEE Transactions on Intelligent Transportation Systems*, vol. 21, no. 6, pp. 2376–2385, 2020. <https://doi.org/10.1109/TITS.2019.2918176>
- [8] Z. Abdullah, P.M. Heerwan, I.M. Izhar, M.A. Zakaria, "Study the influence of distance in artificial potential field (APF) for autonomous emergency braking system (AEB) on longitudinal motion," *IOP Conference Series: Materials Science and Engineering*, vol. 1068, no. 1, p. 12015, 2021. <https://doi.org/10.1088/1757-899X/1068/1/012015>
- [9] C. Ko, S. Han, M. Choi, K.S. Kim, "Integrated path planning and tracking control of autonomous vehicle for collision avoidance based on model predictive control and potential field," in *2020 20th International Conference on Control, Automation and Systems (ICCAS)*, 2020, pp. 956–961. <https://doi.org/10.23919/ICCAS50221.2020.9268369>
- [10] S. Zhao, J. Zhang, R. Zhou, N. Masoud, J. Li, H. Huang et al., "Human-machine shared driving for vehicle collision avoidance based on Hamilton-Jacobi reachability," *Accident Analysis & Prevention*, vol. 230, p. 108474, 2026. <https://doi.org/10.1016/j.aap.2026.108474>
- [11] A. Zulkifli, M. Heerwan, M. Zakaria, M. Ishak, M.A. Shahrom, B. Kujunni, "Motion planning and tracking trajectory of an autonomous emergency braking pedestrian (AEB-P) system based on different brake pad friction coefficients on dry road surface," *International Journal of Automotive and Mechanical Engineering*, vol. 19, 2022. <https://doi.org/10.15282/ijame.19.3.2022.12.0772>
- [12] J.-J. Zhang, Z.-L. Fang, Z.-Q. Zhang, R.-Z. Gao, S.-B. Zhang, "Trajectory tracking control of nonholonomic wheeled mobile robots using model predictive control subjected to Lyapunov-based input constraints," *International Journal of Control, Automation and Systems*, vol. 20, no. 5, pp. 1640–1651, 2022. <https://doi.org/10.1007/s12555-019-0814-x>
- [13] A. Zulkifli, M.H. Peeie, M.A. Zakaria, M.I. Ishak, M.A. Shahrom, B. Kujunni, "Motion planning and tracking trajectory of an autonomous emergency braking pedestrian (AEB-P) system based on different brake pad friction coefficients on dry road surface," *International Journal of Automotive and Mechanical Engineering*, vol. 19, no. 3, pp. 10002–10013, 2022. <https://doi.org/10.15282/ijame.19.3.2022.12.0772>
- [14] X. Chen, S. Li, L. Li, W. Zhao, S. Cheng, "Longitudinal-lateral-cooperative estimation algorithm for vehicle dynamics states based on adaptive-square-root-cubature-Kalman-filter and similarity-principle," *Mechanical Systems and Signal Processing*, vol. 176, p. 109162, 2022. <https://doi.org/10.1016/j.ymssp.2022.109162>
- [15] L. Wang, H. Pang, P. Wang, M. Liu, C. Hu, "A yaw stability-guaranteed hierarchical coordination control strategy for four-wheel drive electric vehicles using an unscented Kalman filter," *Journal of the Franklin Institute*, vol. 360, no. 13, pp. 9663–9688, 2023, doi: <https://doi.org/10.1016/j.jfranklin.2023.06.048>
- [16] B. Kunjunni, M.A. Zakaria, A.P.P. Majeed, A.F.A. Nasir, M.H. Peeie, U.Z. Abdul Hamid, "Effect of load distribution on longitudinal and lateral forces acting on each wheel of a compact electric vehicle," *SN Applied Sciences*, vol. 2, pp. 1–8, 2020. <https://doi.org/10.1007/s42452-020-1996-9>
- [17] A.K. Patra, "Backstepping LQG controller design for stabilizing and trajectory tracking of vehicle suspension system," *SN Applied Sciences*, vol. 2, no. 2, p. 190, 2020. <https://doi.org/10.1007/s42452-020-1945-7>
- [18] Z. WAJID et al., "Robust path tracking of autonomous vehicle in presence of model uncertainties via model based linear quadratic gaussian (LQG) control with adaptive Q-Matrix," vol. 20, p. 10, 2024.
- [19] A. Mitov, J. Kraleov, T. Slavov, I. Angelov, "Comparison of model predictive control (MPC) and linear-quadratic gaussian (LQG) algorithm for electrohydraulic steering control system," in *E3S web of conferences*, EDP Sciences, 2020, p. 04001. <https://doi.org/10.1051/e3sconf/202020704001>
- [20] A. Zulkifli, M.H. Peeie, M.I. Ishak, M.A. Zakaria, "Linear quadratic gaussian (LQG) lateral controller for vehicle collision avoidance trajectory tracking with the presence of additional load disturbance and sensor noise," in *2025 IEEE 8th International Conference on Electrical, Control and Computer Engineering (InECCE)*, 2025, pp. 648–653. <https://doi.org/10.1109/InECCE64959.2025.11150779>
- [21] S.S. Lodhi, N. Kumar, P.K. Pandey, "Autonomous vehicular overtaking maneuver: A survey and taxonomy," *Vehicular Communications*, vol. 42, p. 100623, 2023. <https://doi.org/10.1016/j.vehcom.2023.100623>
- [22] U.Z.A. Hamid, Y. Saito, P. Raksincharoensak, "Collision avoidance performance analysis of a varied loads autonomous vehicle using integrated nonlinear controller," *PERINTIS eJournal*, vol. 8, no. 1, pp. 25–43, 2018.
- [23] L. Gao, C. Beal, J. Mitrovich, S. Brennan, "Vehicle model predictive trajectory tracking control with curvature and friction preview," *IFAC-PapersOnLine*, vol. 55, no. 24, pp. 221–226, 2022. <https://doi.org/10.1016/j.ifacol.2022.10.288>
- [24] I.M. Zulhildi, M.H. Peeie, R.I.M. Eiman, I.M. Izhar, S.M. Asyraf, "Investigation on vehicle dynamic behaviour during emergency braking at different speed," *International Journal of Automotive and Mechanical Engineering*, vol. 16, no. 1, pp. 6161–6172, 2019. <https://doi.org/10.15282/ijame.16.1.2019.6.0468>
- [25] M. Li, M.I. Ishak, P.M. Heerwan, "A numerical simulation of vehicle dynamics behavior for a four-wheel steering vehicle with the passive control system," *Journal of Mechanical Engineering and Sciences*, vol. 16, no. 2, pp. 8953–8964, 2022. <https://doi.org/10.15282/jmes.16.2.2022.12.0708>

- [26] Z. Abdullah, P.M. Heerwan, M.A. Zakaria, M.I. Ishak, "Investigation of brake pad wear impact on autonomous emergency braking pedestrian performance on wet road conditions," *International Journal of Automotive and Mechanical Engineering*, vol. 21, no. 2, pp. 11415–11425, 2024. <https://doi.org/10.15282/ijame.21.2.2024.18.0881>
- [27] B.A.H. Vicente, S.S. James, S.R. Anderson, "Linear system identification versus physical modeling of lateral–longitudinal vehicle dynamics," *IEEE Transactions on Control Systems Technology*, vol. 29, no. 3, pp. 1380–1387, 2021. <https://doi.org/10.1109/TCST.2020.2994120>
- [28] S.L. Brunton, J.N. Kutz, *Data-driven science and engineering: Machine learning, dynamical systems, and control*. Cambridge University Press, 2022.
- [29] A. Garrow, D. L. Peters, S. Bandeddi, "A novel geometric controller for path tracking," *IFAC-PapersOnLine*, vol. 59, no. 30, pp. 497–502, 2025. <https://doi.org/10.1016/j.ifacol.2025.12.286>
- [30] X. Yang, X. Yan, W. Liu, H. Ye, Z. Du, W. Zhong, "An improved stanley guidance law for large curvature path following of unmanned surface vehicle," *Ocean Engineering*, vol. 266, p. 112797, 2022. <https://doi.org/10.1016/j.oceaneng.2022.112797>

Pre-proof copy